

Article

# Analytical Prediction of Balling, Lack-of-Fusion and Keyholing Thresholds in Powder Bed Fusion

Wenjia Wang , Jinqiang Ning  and Steven Y. Liang <sup>\*</sup>

George W. Woodruff School of Mechanical Engineering, Georgia Institute of Technology, 801 Ferst Drive NW, Atlanta, GA 30332, USA; jinqiangning@gatech.edu

<sup>\*</sup> Correspondence: wenjia@gatech.edu (W.W.); steven.liang@me.gatech.edu (S.Y.L.)

**Featured Application:** A complete analytical approach was proposed to predict the occurrence of lack-of-fusion, balling, and keyholing defects in laser powder bed fusion. The boundary heat loss was considered in the presented analytical models. The effect of powder bed porosity on thermal property of powder material was considered in the presented analytical model.

**Abstract:** This paper proposes analytical modeling methods for the prediction of balling, lack-of-fusion and keyholing thresholds in the laser powder bed fusion (LPBF) additive manufacturing. The molten pool dimensions were first predicted by a closed-form analytical thermal model. The effects of laser power input, boundary heat loss, powder size distribution and powder packing pattern were considered in the calculation process. The predicted molten pool dimensions were then employed in the calculation of analytical thresholds for these defects. Reported experimental data with different materials were compared to predictions to validate the presented analytical models. The predicted thresholds of these defects under various process conditions have good agreement with the experimental results. The computation time for the presented models is less than 5 min on a personal computer. The optimized process window for Ti6Al4V was obtained based on the analytical predictions of these defects. The sensitivity analyses of the value of threshold to the laser power and scanning speed were also conducted. The proposed analytical methods show higher computational efficiency than finite element methods, without including any iteration-based computations. The acceptable predictive accuracy and low computational time will make the proposed analytical strategy be a good tool for the optimization of process conditions for the fabrication of defects-free complex products in laser powder bed fusion.

**Keywords:** analytical prediction; boundary heat transfer; powder size distribution; lack of fusion; balling behavior; keyholing defect



**Citation:** Wang, W.; Ning, J.; Liang, S.Y. Analytical Prediction of Balling, Lack-of-Fusion and Keyholing Thresholds in Powder Bed Fusion. *Appl. Sci.* **2021**, *11*, 12053. <https://doi.org/10.3390/app112412053>

Academic Editor: Michele Cali

Received: 24 October 2021

Accepted: 24 November 2021

Published: 17 December 2021

**Publisher's Note:** MDPI stays neutral with regard to jurisdictional claims in published maps and institutional affiliations.



**Copyright:** © 2021 by the authors. Licensee MDPI, Basel, Switzerland. This article is an open access article distributed under the terms and conditions of the Creative Commons Attribution (CC BY) license (<https://creativecommons.org/licenses/by/4.0/>).

## 1. Introduction

Laser powder bed fusion (LPBF) additive manufacturing has been proved to have superior advantages in fabricating products with complex geometries when compared with traditional manufacturing techniques [1,2]. However, the defects occurring in the additive manufacturing process have serious detrimental effects on the quality of the final products and will limit the wide application of this kind of manufacturing technique [3,4]. Thus, good prediction methods for the occurrence of the defects will be very helpful to figure out the suitable process conditions to fabricate products without defects. Lack-of-fusion is a common defect in LPBF which is induced by incomplete melting of powders and incomplete overlap of adjacent molten pools [5,6], which will finally lead to lack-of-fusion porosity in products. Balling behavior is another kind of defect which is mainly caused by the poor wetting between solidified molten pools and the solid substrate, which will lead to unstable and discontinuous melting tracks [7,8]. Severe balling defect can cause high surface roughness and porosity in the final products. Keyholing behavior is a defect

occurring under very high laser energy-density regime. It is related to the evaporation of components in molten material, which will produce gas in the molten pool. Some gas may be trapped by the solidification front of the molten pool, which will lead to high porosity in the final product [1,9]. This paper focuses on the prediction of the generation of the three kinds of defects in laser powder bed fusion.

Experimental, numerical, and analytical methods have been developed by researchers to investigate the mechanisms of the generation of the defects in the additive manufacturing process. Dilip et al. [10] investigated the influence of process conditions on the melting tracks, molten pool shapes and porosity of Ti6Al4V in selective laser melting with the help of SEM images and optical photographs. Cunningham et al. [1] employed ultrahigh-speed X-ray imaging to study the keyhole formation mechanism in additive manufacturing. Shrestha et al. [11] investigates the keyhole-induced porosity by the micro-CT analysis. Zhao et al. [12] used the technique of high-speed X-ray imaging and diffraction to study the in-situ formation process of keyhole pores and molten pools in laser powder bed fusion systems. Bayat et al. [13] employed X-ray computed tomography to study the keyhole-induced pores in powder bed fusion. These experimental techniques have offered some valuable information on the formation process of defects. However, the high cost of the experimental equipment and complex measurement procedures limit the wide adoption of these techniques.

To avoid the inconvenience of the experimental measurements, some researchers employed numerical methods to study the defects formation and their influence on the performance of the products. Bayat et al. [13] developed a numerical model to study the keyhole pores formation and keyhole-induced porosity in powder bed fusion processes. Bruna-Russo et al. [14] proposed a finite element-based thermal model for the calculation of molten pool dimensions and employed the predicted molten pool to study the occurrence of lack-of-fusion defect. Lee et al. [15] presented a numerical simulation strategy to study the temperature profile and molten pool size in powder bed fusion. The powder bed packing pattern was considered in the simulation by a discrete element method. Khairallah et al. [16] employed a 3D powder-scale model to study the mechanisms of pores formation in powder bed fusion processes. Although numerical methods can avoid the high cost on experimental equipment, the high computational cost is still a fatal drawback.

Analytical modeling methods have obtained significant interest from researchers due to their acceptable accuracy and high computational efficiency in the prediction of temperature distribution, molten pool dimensions and related defects in AM. Elsen et al. [17] summarized several thermal models for the prediction of temperature profiles in laser processing techniques. Ning et al. [18] proposed a closed-form temperature prediction model for AM processes, which could consider the boundary conditions. Ji et al. [19] proposed a physics-based analytical modeling approach to calculate the grain size in the products fabricated by additive manufacturing. Ning et al. [20] employed an analytical thermal model to predict the molten pool size in metal additive manufacturing and then correlated the molten pool size with the part porosity evolution by regression analysis. Ning et al. [5] developed an analytical strategy to calculate the lack-of-fusion porosity in powder bed fusion processes, considering the influence of un-melted powders on the final porosity of the products. Promopattum et al. [8] improved Rosenthal's thermal equation by using a heat source with Gaussian distribution and employed the improved thermal model for the prediction of molten pool size. The calculated molten pool geometries were then used as inputs for the prediction of defect generation in additive manufacturing. However, the boundary conditions were not considered in that paper. Moreover, the properties of powder materials were not incorporated. Analytical methods to consider boundary heat loss, effects of powder bed packing on powder material properties are not available yet in the prediction of thresholds for defects formation in LPBF.

In this paper, analytical modeling methods were proposed for the prediction of defects generation in laser powder bed fusion additive manufacturing. The molten pool dimensions were first calculated by an analytical thermal model, with the consideration of heat

input from laser power, heat loss at part boundaries and effect of powder bed porosity (void fraction in the powder bed) on material properties. The predicted molten pool geometries were then employed in the calculation of the thresholds for the lack-of-fusion, balling and keyholing defects to occur. One criterion for the generation of lack-of-fusion defect, one criterion for balling and one criterion for keyholing were employed in this study. The presented analytical methods did not incorporate any iteration-based calculations, which ensure their high computational efficiency. The predicted results were compared to experimental observations of Ti6Al4V, Inconel 718 and 316L stainless steel for validation of the presented analytical models.

## 2. Analytical Modeling

This study proposed analytical modeling methods for the prediction of defects generation in laser powder bed fusion additive manufacturing. The occurrence of lack-of-fusion, balling and keyholing defects were predicted under various process conditions and validated by experimental investigation of Ti6Al4V, Inconel 718 and 316L stainless steel. The molten pool dimensions were first predicted by a temperature prediction model with closed-form solutions. The heat input from power source, boundary heat loss, and the effects of powder bed porosity on the thermal properties were considered in the calculation process. The powder bed porosity was calculated by an advancing front approach based on the information of powder size distribution and powder packing pattern. The predicted molten pool dimensions were then employed into the calculation of thresholds for the lack-of-fusion, balling and keyholing defects.

The analytical thermal model employed in this study consists of a linear heat input solution and a linear heat loss solution. A point moving heat source model is employed as the heat input solution, which was developed by Carslaw and Jaeger based on the assumption of semi-infinite medium [21]. The heat input solution was used to calculate the temperature increase due to the heat input from power source; it can be expressed as

$$\theta_{laser}(x, y, z) = \frac{P\eta}{2\pi kR(T_m - T_0)} \exp\left(\frac{-V(R+x)}{2\kappa}\right) \quad (1)$$

where  $T_m$  denotes the melting point,  $T_0$  represents the room (initial) temperature, and  $\theta_{laser} = \frac{T-T_0}{T_m-T_0}$  represents the dimensionless temperature.  $P$  and  $V$  represent the process conditions, which are laser power and scanning speed.  $\eta$  is the absorptivity of the laser power.  $\kappa = \frac{k}{\rho c}$  is the thermal diffusivity of material, which can be calculated with the information of density  $\rho$ , specific heat  $c$  and thermal conductivity  $k$ .  $R = \sqrt{x^2 + y^2 + z^2}$  represents the distance from the calculated location to the laser source.

The heat loss solution was used to consider the temperature drop due to the boundary heat transfer, which was derived from the point moving heat source model with equivalent power loss and zero moving velocity. The mechanisms of boundary heat loss in the process of laser powder bed fusion additive manufacturing are shown in Figure 1. The blue arrows above the part represent the thermal radiation and convection from the part to the ambience, which has obvious influence on the temperature profile in the part. The red arrow denotes the laser power source. The purple arrow on the part represents the scanning direction of the heat source. To calculate the heat loss at boundaries, the boundary surfaces are discretized into plenty of small rectangular sections, as shown in Figure 1. Each section can be considered as a small heat sink with equivalent heat loss as a stationary point heat source at its center. Thus, the equivalent heat loss from thermal radiation and convection [5] can be expressed as

$$Q_{conv} = Ah(T - T_0) \quad (2)$$

$$Q_{rad} = A\varepsilon\sigma(T^4 - T_0^4) \quad (3)$$

where  $Q_{conv}$  is the boundary heat loss through thermal convection, and  $Q_{rad}$  is the boundary heat loss through thermal radiation.  $h$  is the heat transfer coefficient, and  $\epsilon$  is the emissivity.  $\sigma$  represents the Stefan–Boltzmann constant, of which the value is  $5.67 \times 10^{-8} \text{ W}/(\text{m}^2 \cdot \text{K}^4)$ .  $T_0$  represents the initial temperature,  $T$  is the temperature of each heat sink center, which can be obtained through the heat input solution.  $A$  is the surface area of each heat sink.

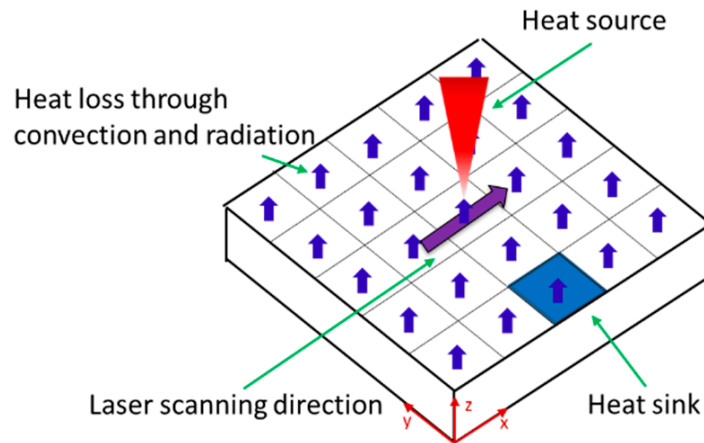


**Figure 1.** Mechanisms of heat transfer in LPBF. The red arrow represents the heat source, the blue arrows represent the heat loss through convection and radiation to the ambience. The purple arrow shows the scanning direction of the laser. The small squares are heat sinks on the top surface [5,18].

Then, the temperature drop due to the thermal radiation and convection [5] can be expressed as

$$\theta_{loss}(x, y, z) = \sum_{i=1}^n \frac{A_i}{2\pi k R_i (T_m - T_0)} \left[ h(T_i - T_0) + \epsilon \sigma (T_i^4 - T_0^4) \right] \quad (4)$$

In this equation, the  $i$  represents the index of heat sinks on the top surface of the part, and  $n$  is the total number of the sinks. The total temperature distribution in the part can be obtained by the superposition of the linear heat input solution and linear heat loss solution, which can be expressed as the following equation

$$\theta(x, y, z) = \theta_{laser} - \theta_{loss} \quad (5)$$

The molten pool dimensions were determined by comparing the temperature profile with the melting temperature of the material.

The effect of powder bed porosity on the thermal properties of the powders was also considered in the prediction of temperature profile and molten pool geometries. An advancing front approach was employed to compute the powder bed porosity based on the information of powder size distribution and powder packing. Several assumptions are enforced in this approach. First, the shape of the powders is assumed to be a circle. Second, the powder bed is assumed to have the maximum packing density in the manufacturing process. Third, this approach calculates the packing porosity in a 2D domain. Figure 2 shows the strategy of the advancing front approach. Three circles are generated first as the initial front. The following circles are generated based on the initial front along the positive directions of the blue vectors, as shown in Figure 2. It should be noted that the positive direction of the vector is along the anti-clockwise direction. The generated circles show the densest packing pattern in this 2D domain [22]. The effect of powder bed porosity on the thermal conductivity of the powder material was developed in [23], which can be expressed as

$$k_p = \frac{k_s(1 - \epsilon)}{1 + \psi \frac{k_s}{k_g}} \quad (6)$$

$$\psi = 0.02 \times 10^{2(\epsilon-0.3)} \tag{7}$$

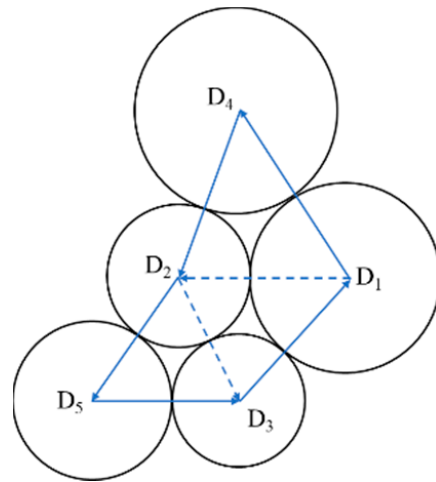


Figure 2. Generation process of powder packing pattern using advancing front approach [22].

In this equation,  $k_p$ ,  $k_s$  and  $k_g$  represent the thermal conductivity of powders, solid material and gas, respectively. For Argon,  $k_g = 0.0176$  (W/mK).  $\epsilon$  represents the void fraction of the powder bed, and  $\psi$  denotes a factor in the calculation process [24].

Lack-of-fusion defect is induced by incomplete melting of powders. The threshold for the lack-of-fusion defect was first developed by Tang et al. in [6], with the assumption of dual half-ellipse molten pool shapes. This threshold can be expressed as

$$\frac{H^2}{W^2} + \frac{L^2}{D^2} \leq 1 \tag{8}$$

In this equation,  $H$  and  $L$  represent the hatching space and layer thickness, respectively.  $W$  and  $D$  represent the molten pool width and depth, respectively. When the equation is not satisfied, the lack-of-fusion defect will occur in the manufacturing process.

The balling defect usually happens in the low energy density regime, and it is caused by the poor wettability of the molten pools to the solid substrate. The threshold for the occurrence of balling behavior was proposed in [25], which can be expressed as

$$\frac{\pi w}{l} > 1 \tag{9}$$

where  $w$  and  $l$  represent the molten pool width and length, respectively. The balling defect will occur when the equation is not satisfied.

The keyholing defect is related to the evaporation of materials during the manufacturing process. A criterion for the generation of the keyholing defect was developed in [26], which can be expressed as

$$\frac{\Delta H}{h_s} = \frac{AP}{\pi h_s \sqrt{Dua^3}}, h_s = \rho C_p T_m \tag{10}$$

$$\frac{\Delta H}{h_s} > \frac{\pi T_b}{T_m} \tag{11}$$

In this equation,  $\frac{\Delta H}{h_s}$  represents normalized enthalpy, with  $\Delta H$  as the specific enthalpy and  $h_s$  as enthalpy of melting.  $P$  and  $u$  are the process conditions, which are the laser power and scanning speed.  $A$  denotes the absorption coefficient of laser power, and  $a$  represents the diameter of the laser beam.  $T_m$  and  $T_b$  represent the melting temperature and boiling point of the material, and  $D$  and  $C_p$  are the thermal diffusivity and specific

heat, respectively. The keyholing defect will form in manufacturing process when the Equation (11) is satisfied.

### 3. Experimental Validation and Discussion

This study proposes analytical methods to predict the defect generation in laser powder bed fusion additive manufacturing. The occurrence of lack-of-fusion, balling and keyholing defects were predicted under various combinations of process conditions and validated by experimental study of different materials. All the experimental data used in this study are adopted from the literature. The prediction accuracy of the proposed analytical thermal model has been validated in previous papers of our group. The presented model has shown acceptable accuracy in the prediction of molten pool dimensions in powder bed fusion. Furthermore, it has been validated that the consideration of boundary heat loss can improve the prediction accuracy for the molten pool dimensions [18]. Table 1, Table 2 and Table 5 show the predicted molten pool dimensions for three different materials under various process conditions. The energy density in the table is defined as

$$\frac{\text{Power}}{\text{Speed} \times \text{hatch space} \times \text{layer thickness}}$$

**Table 1.** Results of lack-of-fusion for Ti6Al4V [27].

Power (W)	Scanning Speed (mm/s)	Computed Molten Pool Depth ( $\mu\text{m}$ )	Computed Molten Pool Width ( $\mu\text{m}$ )	Energy Density ( $\text{J}/\text{mm}^3$ )	Measured Porosity (%)	$\frac{H^2}{W^2} + \frac{L^2}{D^2}$
40	1200	20.2	38.1	11.1	22.6	9.1
40	1080	22.2	42.1	12.3	19.5	7.5
40	960	24.2	46.1	13.9	17.7	6.2
40	840	24.2	50.1	15.9	15.1	5.5
40	720	28.3	54.1	18.5	11.9	4.5
40	600	30.3	58.1	22.2	9.3	3.9
40	480	34.3	66.1	27.8	4.7	3.0
40	360	38.4	74.1	37.0	2.4	2.4
40	240	44.4	90.2	55.6	0.7	1.7
40	120	56.6	114.2	111.1	0.6	1.0

For the prediction of the formation of lack-of-fusion defect, Ti6Al4V and Inconel 718 were employed as the materials. Tables 1 and 2 show the process conditions for Ti6Al4V and Inconel 718, respectively. Table 3 shows the thermal properties of Ti6Al4V and Inconel 718. The powder size distributions of the two materials are shown in Figure 3. With the advancing front approach, the powder packing pattern was obtained, as shown in Figure 4. By image analysis of the packing pattern using Image J, the porosity of the powder bed was calculated, as shown in Table 4. To investigate the influence of the powder numbers on the calculation of powder bed porosity, the porosity was calculated at least triple under different levels of powder number. From the results, it shows that the influence of powder number is negligible during the calculation of powder bed porosity. The average porosities were used in this study, which is 12.88% for Ti6Al4V and 13.47% for Inconel 718.

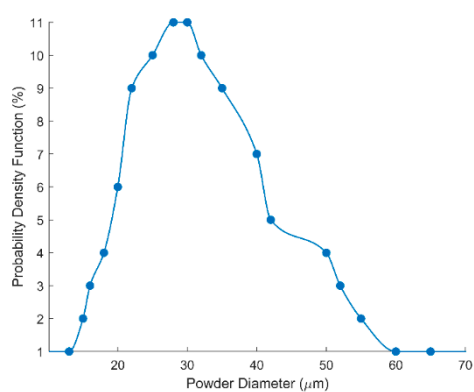
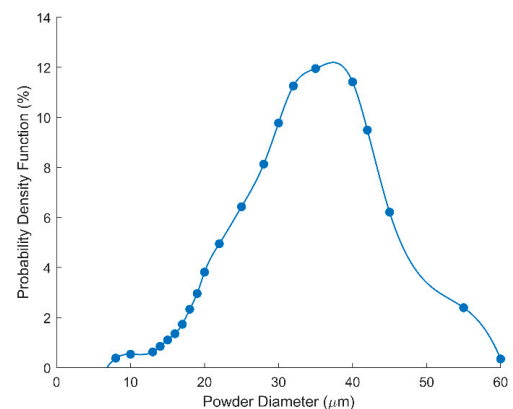
With the results of molten pool geometries, the lack-of-fusion thresholds were computed. The calculated results are shown in Tables 1 and 2, which is  $110 \text{ J}/\text{mm}^3$  for Ti6Al4V and  $160 \text{ J}/\text{mm}^3$  for Inconel 718. To validate the prediction accuracy of the proposed analytical methods, the predicted thresholds were compared with experimental measurements, as shown in Figure 5. The predicted results have good agreements with experimental data for the two materials.

**Table 2.** Results of lack-of-fusion and keyholing for Inconel 718 [28].

Power (W)	Scanning Speed (mm/s)	Computed Molten Pool Depth ( $\mu\text{m}$ )	Computed Molten Pool Width ( $\mu\text{m}$ )	Energy Density ( $\text{J}/\text{mm}^3$ )	Measured Porosity (%)	$\frac{H^2}{W^2} + \frac{L^2}{D^2}$	$\frac{\Delta H}{h_s}$
90	1600	14.1	26.1	28.1	13.4	12.6	1.7
90	1200	18.2	34.1	37.5	3.8	7.4	2.0
90	800	24.2	46.1	56.3	0.3	4.1	2.4
90	600	28.3	54.1	75.0	0.4	3.0	2.8
90	400	38.4	74.1	112.5	0.4	1.6	3.4
90	300	46.5	90.2	150.0	0.5	1.1	4.0
90	200	60.6	118.2	225.0	0.9	0.6	4.9
90	100	88.9	174.3	450.0	5.9	0.3	6.9

**Table 3.** Material properties of Ti6Al4V [6,29,30], Inconel 718 [8] and SS316L [6,31].

Name	Symbol	Ti6Al4V	Inconel 718	SS316L	Unit
Density	$\rho$	4428	8220	7633	$\text{kg}/\text{m}^3$
Thermal conductivity	$k$	18.4	11	25	$\text{W}/(\text{m}\cdot^\circ\text{C})$
Specific heat	$c$	517	420	594	$\text{J}/(\text{kg}\cdot^\circ\text{C})$
Absorption	$\eta$	0.48	0.4	0.35	1
Room temperature	$T_0$	20	20	20	$^\circ\text{C}$
Boiling temperature	$T_b$	/	2917	/	$^\circ\text{C}$
Melting temperature	$T_m$	1655	1336	1400	$^\circ\text{C}$
Heat convection coefficient	$h$	24	25	24	$\text{W}/(\text{m}^2\cdot^\circ\text{C})$
Emissivity	$\varepsilon$	0.9	0.8	0.26	1

**(a)****(b)****Figure 3.** Powder size information. (a) Powder size distribution of Ti6Al4V [27]. (b) Powder size distribution of Inconel 718 [28].**Table 4.** Powder bed porosity.

Powder Number	Powder Bed Porosity (%)	
	Inconel 718	Ti6Al4V
100	13.66	12.87
200	14.01	13.21
300	13.96	12.62
400	13.29	12.76
500	12.41	12.95
Average	13.47	12.88

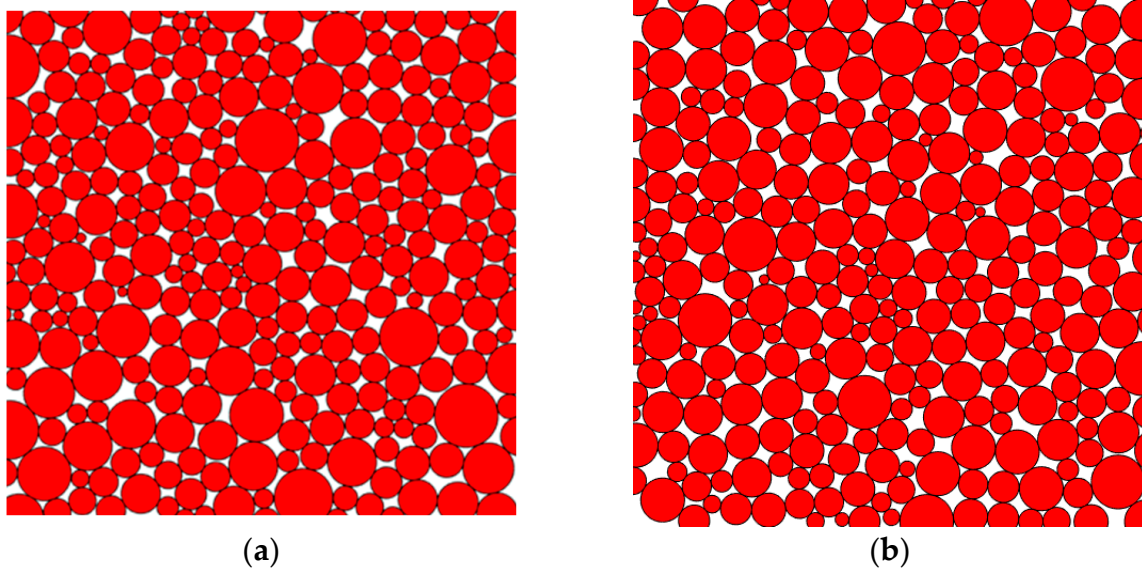


**Figure 4.** Powder packing pattern with 300 powders. (a) Ti6Al4V, (b) Inconel 718.

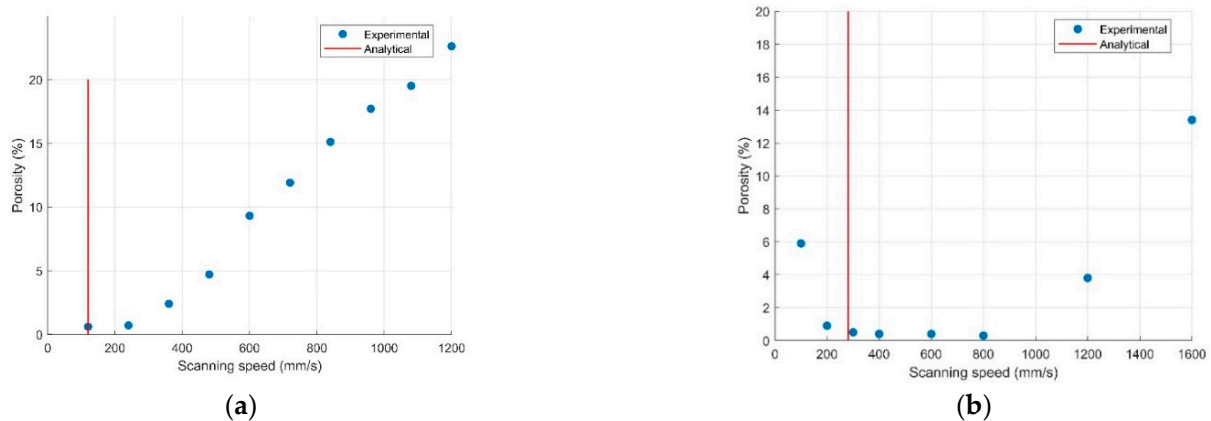


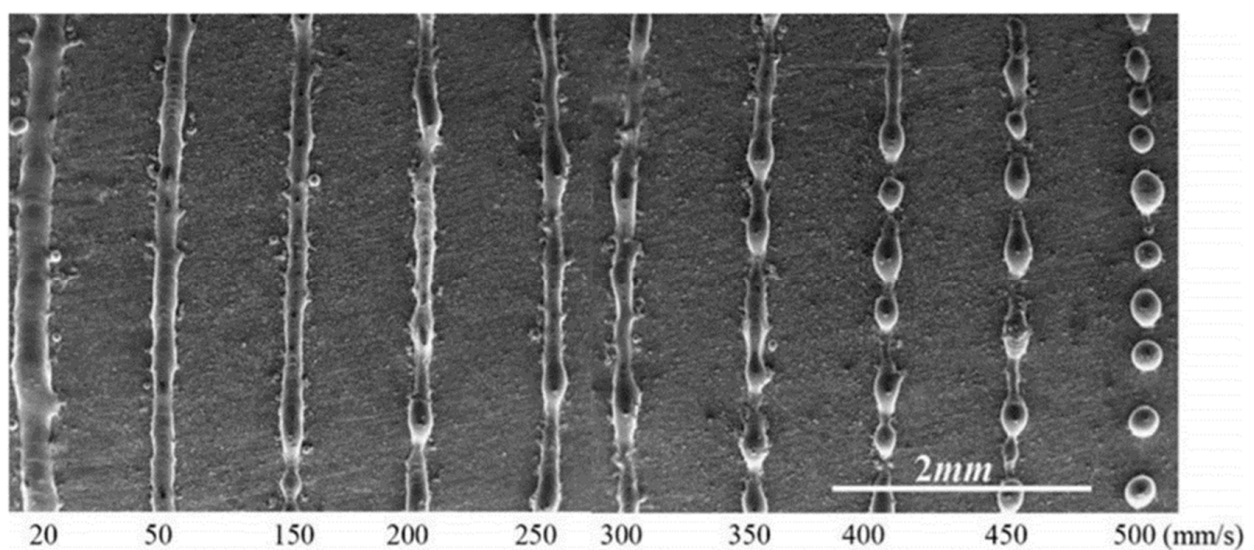
**Figure 5.** Predicted thresholds for lack-of-fusion defect. (a) Ti6Al4V, (b) Inconel 718 [27,28].

The thresholds for the balling defect were calculated with the information of the predicted molten pool width and length. The 316L stainless steel was used to validate the proposed analytical method for balling prediction. The boundary heat loss and effects of powder bed porosity were not considered in this calculation, because the information of part size and powder size distribution were not given in the reference paper. Table 3 shows the thermal properties of 316L. Table 5 shows the process conditions and predicted results. The experimental observation of balling behavior is shown in Figure 6. The balling defect becomes obvious when the scanning speed is over 350 mm/s, which is very close to the predicted result.

The prediction for the occurrence of keyholing defect was carried out with the information of material properties and process conditions. The calculated results are shown in Tables 2 and 6. The predicted thresholds are 5.4 for Ti6Al4V and 6.2 for Inconel 718. The comparison of experimental results and analytical predictions are shown in Figure 7. Acceptable agreement can be observed between experimental results and analytical predictions.

**Table 5.** Results of balling for 316L.

Power (W)	Scanning Speed (mm/s)	Computed Molten Pool Width ( $\mu\text{m}$ )	Computed Molten Pool Length ( $\mu\text{m}$ )	$\frac{\pi w}{l}$
190	20	427.1	481.0	2.8
190	50	306.5	424.8	2.3
190	150	185.9	372.7	1.6
190	200	155.8	362.7	1.3
190	250	135.7	354.7	1.2
190	300	125.6	350.7	1.1
190	350	105.5	346.7	1.0
190	400	105.5	342.7	1.0
190	450	95.5	340.7	0.9
190	500	85.4	338.7	0.8

**Figure 6.** Experimental observation of single tracks for 316L [32].**Table 6.** Results of keyholing for Ti6Al4V [10].

Power (W)	Scanning Speed (mm/s)	Energy Density ( $\text{J}/\text{mm}^3$ )	Measured Porosity (%)	$\frac{\Delta H}{h_s}$
50	500	33	22.1	1.5
50	750	22	44.4	1.2
50	1000	16	55.1	1.0
50	1200	13	64.6	0.9
100	500	66	0	2.9
100	750	44	5.6	2.4
100	1000	33	19.6	2.1
100	1200	27	25.2	1.9
150	500	100	7.8	4.4
150	750	66	0	3.6
150	1000	50	0	3.1
150	1200	41	5.1	2.8
195	500	130	9.2	5.7
195	750	86	2.3	4.7
195	1000	65	0	4.1
195	1200	54	0	3.7

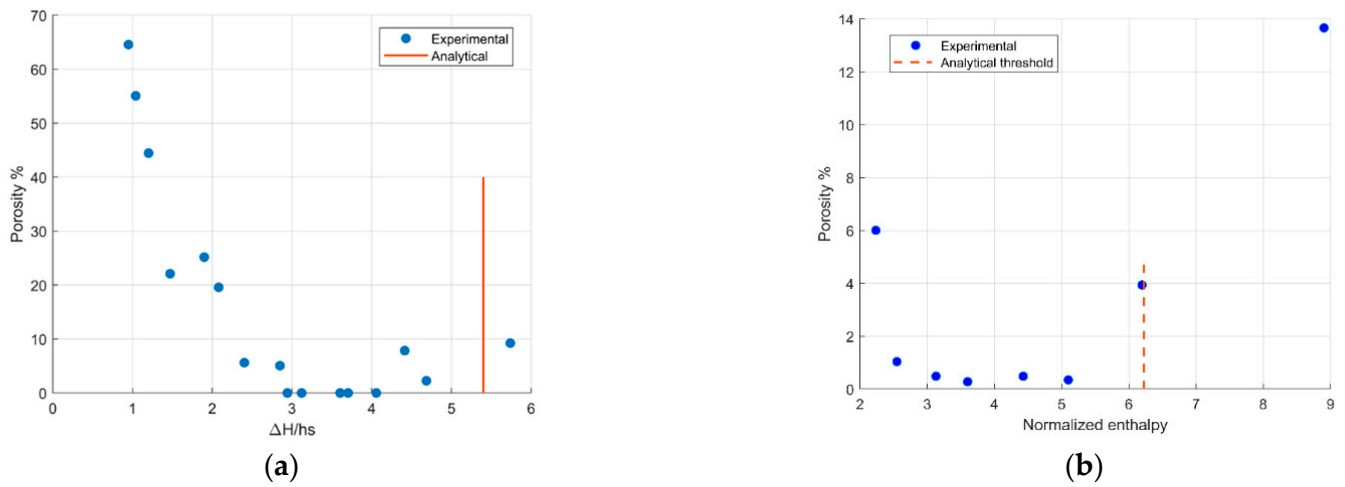


Figure 7. Validation of keyholing threshold prediction. (a) Ti6Al4V. (b) Inconel 718.

The sensitivity of the threshold models for the lack-of-fusion, balling and keyholing defects to the laser power and scanning speed were also carried out. The detailed results are shown in Figures 8 and 9. It can be observed that the value of the balling threshold formula and lack-of-fusion formula have a negative relationship with the laser power, while the keyhole formula has a positive relationship with the laser power. As for sensitivity to scanning speed, the balling formula and keyhole formula have negative relationships with scanning speed, while lack-of-fusion formula has a positive relationship with scanning speed.

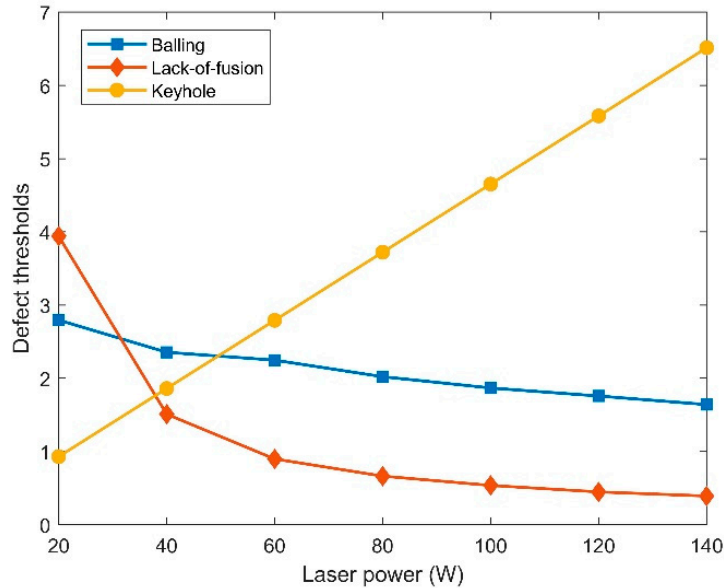


Figure 8. Sensitivity of thresholds to laser power.

The process window of the Ti6Al4V in laser powder-bed fusion additive manufacturing was also predicted by the presented analytical models. The laser power changes from 20 W to 200 W, with 20 W as an increment. The scanning speed changes from 200 mm/s to 1400 mm/s, with 200 mm/s as an increment. Table 7 shows the detailed prediction for defects under various process conditions. This table can be used to optimize the suitable process conditions for the fabrications of products without any defects.

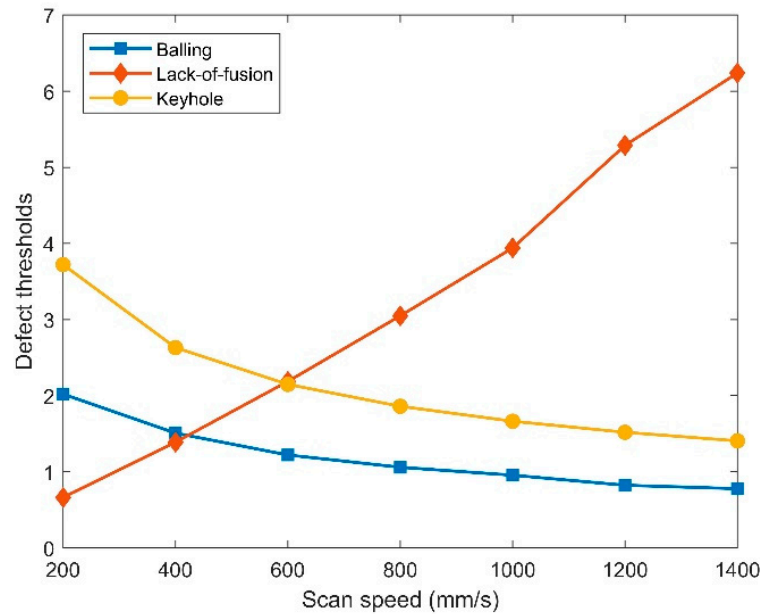


Figure 9. Sensitivity of thresholds to scan speed.

Table 7. Process window of the Ti6Al4V. LOF represents lack-of-fusion defect.

Power (W)	Scanning Speed (mm/s)						
	200	400	600	800	1000	1200	1400
20	LOF	LOF	LOF	LOF	LOF	LOF	LOF
40	LOF	LOF	LOF	LOF	LOF	LOF	LOF
60	No	LOF	LOF	LOF	LOF	LOF	Balling
80	No	LOF	LOF	LOF	Balling	Balling	Balling
100	No	LOF	LOF	Balling	Balling	Balling	Balling
120	Keyhole	No	LOF	Balling	Balling	Balling	Balling
140	Keyhole	No	Balling	Balling	Balling	Balling	Balling
160	Keyhole	No	Balling	Balling	Balling	Balling	Balling
180	Keyhole	Keyhole	Balling	Balling	Balling	Balling	Balling
200	Keyhole	Keyhole	Balling	Balling	Balling	Balling	Balling

The presented analytical models in this study have been validated by experimental measurements of different materials under various process conditions. In addition, the computational time for the presented models on a personal computer is less than five minutes, which shows their high computational efficiency. In the future, the temperature-dependent material properties and sensitivity to laser power absorption can be considered in the calculation process so as to improve the prediction accuracy of these analytical models. The proposed analytical modeling method can be a promising tool for future study of manufacturing conditions for large and complex products.

#### 4. Conclusions

In this paper, analytical modeling methods are proposed to predict the defect generation in laser powder bed fusion additive manufacturing, without relying on iteration-based computation. The thresholds for the generation of lack-of-fusion, balling and keyholing defects were predicted under various process conditions. The molten pool dimensions in the additive manufacturing process were first calculated by a closed-form analytical thermal model. The heat input from laser source, heat loss at part boundaries and effect of powder bed porosity on thermal properties were considered in the thermal model. The obtained molten pool information was then employed in the calculation of the thresholds

for defects. One criterion for the calculation of threshold for lack-of-fusion defect was presented; one criterion for balling and one criterion for keyholing were also proposed.

The experimental investigations of Ti6Al4V, Inconel 718 and 316L in powder bed fusion were employed to validate the proposed analytical methods. The predicted thresholds of these defects have good agreement with experimental results. The computational time for the presented models is less than five minutes on a personal computer with a Intel i5 processor running at 3.4 GHz. The balling threshold has negative relationships with both laser power and scan speed. The lack-of-fusion threshold has negative and positive relationships with power and speed, respectively. The keyholing threshold holds positive and negative relationships with power and speed, respectively. The acceptable prediction accuracy and high computational efficiency of the proposed methods will make them good tools for the optimization of process conditions in powder bed fusion. Furthermore, the presented models can be a good basis for future research on the prediction of defects of complex parts in additive manufacturing.

**Author Contributions:** Conceptualization, W.W. and J.N.; methodology, W.W.; software, W.W.; validation, W.W., J.N. and S.Y.L.; formal analysis, W.W.; investigation, W.W.; resources, S.Y.L.; data curation, W.W.; writing—original draft preparation, W.W.; writing—review and editing, W.W., J.N. and S.Y.L.; visualization, W.W.; supervision, S.Y.L.; project administration, S.Y.L.; funding acquisition, S.Y.L. All authors have read and agreed to the published version of the manuscript.

**Funding:** This research received no external funding.

**Institutional Review Board Statement:** Not applicable.

**Informed Consent Statement:** Not applicable.

**Data Availability Statement:** Not applicable.

**Conflicts of Interest:** The authors declare no conflict of interest.

## References

1. Cunningham, R.; Zhao, C.; Parab, N.; Kantzos, C.; Pauza, J.; Fezzaa, K.; Sun, T.; Rollett, A.D. Keyhole threshold and morphology in laser melting revealed by ultrahigh-speed x-ray imaging. *Science* **2019**, *363*, 849–852. [[CrossRef](#)]
2. Hojjatzadeh, S.M.H.; Parab, N.D.; Yan, W.; Guo, Q.; Xiong, L.; Zhao, C.; Qu, M.; Escano, L.L.; Xiao, X.; Fezzaa, K.; et al. Pore elimination mechanisms during 3D printing of metals. *Nat. Commun.* **2019**, *10*, 1–8. [[CrossRef](#)]
3. Sheridan, L.; Scott-Emuakpor, O.E.; George, T.; Gockel, J.E. Relating porosity to fatigue failure in additively manufactured alloy 718. *Mater. Sci. Eng. A* **2018**, *727*, 170–176. [[CrossRef](#)]
4. Tang, M.; Pistorius, P.C. Oxides, porosity and fatigue performance of AlSi10Mg parts produced by selective laser melting. *Int. J. Fatigue* **2017**, *94*, 192–201. [[CrossRef](#)]
5. Ning, J.; Wang, W.; Zamorano, B.; Liang, S.Y. Analytical modeling of lack-of-fusion porosity in metal additive manufacturing. *Appl. Phys. A* **2019**, *125*, 1–11. [[CrossRef](#)]
6. Tang, M.; Pistorius, P.C.; Beuth, J.L. Prediction of lack-of-fusion porosity for powder bed fusion. *Addit. Manuf.* **2017**, *14*, 39–48. [[CrossRef](#)]
7. Wang, D.; Liu, Y.; Yang, Y.; Xiao, D. Theoretical and experimental study on surface roughness of 316L stainless steel metal parts obtained through selective laser melting. *Rapid Prototyp. J.* **2016**, *22*, 706–716. [[CrossRef](#)]
8. Promopatum, P.; Yao, S.C. Analytical evaluation of defect generation for selective laser melting of metals. *Int. J. Adv. Manuf. Technol.* **2019**, *103*, 1185–1198. [[CrossRef](#)]
9. Vastola, G.; Pei, Q.X.; Zhang, Y.W. Predictive model for porosity in powder-bed fusion additive manufacturing at high beam energy regime. *Addit. Manuf.* **2018**, *22*, 817–822. [[CrossRef](#)]
10. Dilip, J.J.S.; Zhang, S.; Teng, C.; Zeng, K.; Robinson, C.; Pal, D.; Stucker, B. Influence of processing parameters on the evolution of melt pool, porosity, and microstructures in Ti-6Al-4V alloy parts fabricated by selective laser melting. *Prog. Addit. Manuf.* **2017**, *2*, 157–167. [[CrossRef](#)]
11. Shrestha, S.; Starr, T.; Chou, K. A study of keyhole porosity in selective laser melting: Single-track scanning with micro-CT analysis. *J. Manuf. Sci. Eng.* **2019**, *141*, 071004. [[CrossRef](#)]
12. Zhao, C.; Fezzaa, K.; Cunningham, R.W.; Wen, H.; De Carlo, F.; Chen, L.; Rollett, A.D.; Sun, T. Real-time monitoring of laser powder bed fusion process using high-speed X-ray imaging and diffraction. *Sci. Rep.* **2017**, *7*, 1–11. [[CrossRef](#)]
13. Bayat, M.; Thanki, A.; Mohanty, S.; Witvrouw, A.; Yang, S.; Thorborg, J.; Tiedje, N.S.; Hattel, J.H. Keyhole-induced porosities in Laser-based Powder Bed Fusion (L-PBF) of Ti6Al4V: High-fidelity modelling and experimental validation. *Addit. Manuf.* **2019**, *30*, 100835. [[CrossRef](#)]

14. Bruna-Rosso, C.; Demir, A.G.; Previtali, B. Selective laser melting finite element modeling: Validation with high-speed imaging and lack of fusion defects prediction. *Mater. Des.* **2018**, *156*, 143–153. [[CrossRef](#)]
15. Lee, Y.S.; Zhang, W. Modeling of heat transfer, fluid flow and solidification microstructure of nickel-base superalloy fabricated by laser powder bed fusion. *Addit. Manuf.* **2016**, *12*, 178–188. [[CrossRef](#)]
16. Khairallah, S.A.; Anderson, A.T.; Rubenchik, A.; King, W.E. Laser powder-bed fusion additive manufacturing: Physics of complex melt flow and formation mechanisms of pores, spatter, and denudation zones. *Acta Mater.* **2016**, *108*, 36–45. [[CrossRef](#)]
17. Van Elsen, M.; Baelmans, M.; Mercelis, P.; Kruth, J.P. Solutions for modelling moving heat sources in a semi-infinite medium and applications to laser material processing. *Int. J. Heat Mass Transf.* **2007**, *50*, 4872–4882. [[CrossRef](#)]
18. Ning, J.; Mirkoohi, E.; Dong, Y.; Sievers, D.E.; Garmestani, H.; Liang, S.Y. Analytical modeling of 3D temperature distribution in selective laser melting of Ti-6Al-4V considering part boundary conditions. *J. Manuf. Process.* **2019**, *44*, 319–326. [[CrossRef](#)]
19. Ji, X.; Mirkoohi, E.; Ning, J.; Liang, S.Y. Analytical modeling of post-printing grain size in metal additive manufacturing. *Opt. Lasers Eng.* **2020**, *124*, 105805. [[CrossRef](#)]
20. Ning, J.; Sievers, D.E.; Garmestani, H.; Liang, S.Y. Analytical modeling of part porosity in metal additive manufacturing. *Int. J. Mech. Sci.* **2020**, *172*, 105428. [[CrossRef](#)]
21. Carslaw, H.; Jaeger, J. *Conduction of Heat in Solids*; Oxford Science Publication: Oxford, UK, 1990.
22. Feng, Y.T.; Han, K.; Owen, D.R.J. Filling domains with disks: An advancing front approach. *Int. J. Numer. Methods Eng.* **2003**, *56*, 699–713. [[CrossRef](#)]
23. Xing, J.; Sun, W.; Rana, R.S.; Senior Member IEEE. 3D modeling and testing of transient temperature in selective laser sintering (SLS) process. *Optik* **2013**, *124*, 301–304. [[CrossRef](#)]
24. Ning, J.; Wang, W.; Ning, X.; Sievers, D.E.; Garmestani, H.; Liang, S.Y. Analytical thermal modeling of powder bed metal additive manufacturing considering powder size variation and packing. *Materials* **2020**, *13*, 1988. [[CrossRef](#)] [[PubMed](#)]
25. Yadroitsev, I.; Gusarov, A.; Yadroitsava, I.; Smurov, I. Single track formation in selective laser melting of metal powders. *J. Mater. Process. Technol.* **2010**, *210*, 1624–1631. [[CrossRef](#)]
26. King, W.E.; Barth, H.D.; Castillo, V.M.; Gallegos, G.F.; Gibbs, J.W.; Hahn, D.E.; Kamath, C.; Rubenchik, A.M. Observation of keyhole-mode laser melting in laser powder-bed fusion additive manufacturing. *J. Mater. Process. Technol.* **2014**, *214*, 2915–2925. [[CrossRef](#)]
27. Gong, H.; Rafi, K.; Gu, H.; Starr, T.; Stucker, B. Analysis of defect generation in Ti-6Al-4V parts made using powder bed fusion additive manufacturing processes. *Addit. Manuf.* **2014**, *1*, 87–98. [[CrossRef](#)]
28. Choi, J.P.; Shin, G.H.; Yang, S.; Yang, D.Y.; Lee, J.S.; Brochu, M.; Yu, J.H. Densification and microstructural investigation of Inconel 718 parts fabricated by selective laser melting. *Powder Technol.* **2017**, *310*, 60–66. [[CrossRef](#)]
29. Yang, Y.; Knol, M.F.; Van Keulen, F.; Ayas, C. A semi-analytical thermal modelling approach for selective laser melting. *Addit. Manuf.* **2018**, *21*, 284–297. [[CrossRef](#)]
30. Roberts, I.A.; Wang, C.J.; Esterlein, R.; Stanford, M.; Mynors, D.J. A three-dimensional finite element analysis of the temperature field during laser melting of metal powders in additive layer manufacturing. *Int. J. Mach. Tools Manuf.* **2009**, *49*, 916–923. [[CrossRef](#)]
31. Philo, A.M.; Mehraban, S.; Holmes, M.; Sillars, S.; Sutcliffe, C.J.; Sienz, J.; Brown, S.G.; Lavery, N.P. A pragmatic continuum level model for the prediction of the onset of keyholing in laser powder bed fusion. *Int. J. Adv. Manuf. Technol.* **2019**, *101*, 697–714. [[CrossRef](#)]
32. Li, R.; Liu, J.; Shi, Y.; Wang, L.; Jiang, W. Balling behavior of stainless steel and nickel powder during selective laser melting process. *Int. J. Adv. Manuf. Technol.* **2012**, *59*, 1025–1035. [[CrossRef](#)]